Spin-dependent transport in uranium

M.-H. Wu,* H. Rossignol, and M. Gradhand
H. H. Wills Physics Laboratory, University of Bristol, Bristol BS8 1TL, United Kingdom

(Received 25 February 2020; revised manuscript received 22 May 2020; accepted 22 May 2020; published 8 June 2020)

Given the challenges in experimental studies of uranium, the heaviest naturally occurring metal, we present first-principles calculation for the spin-dependent transport. Showing the largest atomic spin-orbit coupling we explore the ability of various crystal phases to maximize the charge-to-spin conversion using a fully relativistic Korringa-Kohn-Rostoker Green's function method. The transport theory is based on a semiclassical description where intrinsic and extrinsic, skew scattering, contributions can be separated easily. In addition to the various crystal phases we analyze the effect of substitutional impurities for γ, hcp, as well as the α phase. We predict a very high, 10^4 $(\Omega\,\mathrm{cm})^{-1}$, spin Hall conductivity for the metastable hcp-U phase, a giant value five times larger than for the conventional spin Hall material Pt. We estimated an efficiency of charge-to-spin current conversion of up to 30%. The spin diffusion length, a crucial parameter in any application, is predicted to be in the range from 3 to 6.5 nm, compatible with other charge-to-spin conversion materials. Relating our work to the sparse experimental results, our calculations suggest a γ phase in the thin film rather than the experimentally expected α phase.

DOI: 10.1103/PhysRevB.101.224411

I. INTRODUCTION

The spin Hall effect (SHE) has attracted interest due to its potential application in devices requiring the generation of spin currents such as magnetic random access memory (MRAM) [1–3]. The spin currents generated via SHE in nominally nonmagnetic materials can be exploited to switch the active magnetic layer. In contrast to devices relying on spin injection, the number of ferromagnet/nonmagnet interfaces can be reduced, improving the efficiency of the entire device [4–6]. The microscopic mechanisms of the SHE are typically grouped into intrinsic and extrinsic contributions. The former directly connects to the intrinsic electronic structure of a crystal, and the latter is induced by disordered potentials in the system such as chemical impurities. Since the driving mechanism of the SHE is the relativistic coupling of spin and orbital degrees of freedom, such applications rely on materials maximizing spin-orbit coupling (SOC) [7–11]. For this reason the search is on for materials with strong SOC relevant for the aforementioned applications.

Uranium is a naturally occurring heavy metal and has been investigated or utilized in past decades for its interesting properties [12–20]. It has a strong spin-orbit interaction and a complex phase diagram with several distinct crystal structures such as α (orthorhombic), β (bct), γ (bcc), and hcp phases. Uranium is a light actinide with itinerant $5f$ electrons. This property can be exploited in various configurations such as magnetic multilayer systems [21–25]. The SHE of U was experimentally reported [26] and was found to be surprisingly low. However, theoretical studies are sparse and no understanding of the experimental results has been put forward. This is the motivation for the current work where we investigate U by computational methods for a better understanding of the mechanisms governing the SHE in U.

We will use density functional theory (DFT) and the Korringa-Kohn-Rostoker (KKR) Green's function method to investigate the spin-dependent transport properties of various U phases and the effect of impurities in the bulk phases. In Sec. II, we introduce the structural details of uranium. This will be followed by Sec. III briefly introducing the computational methods in order to account for the intrinsic SHE and extrinsic SHE. All methods have been derived earlier and are discussed in detail in Refs. [27–29] and only the most relevant points will be highlighted here. In Sec. IV A, we present the results of the intrinsic SHE for three bulk phases and the extrinsic SHE for all of them doped with different substitutional impurities. Finally, we will explore the various relevant parameters such as the spin diffusion length as well as the impurity concentration in such systems making contact to the existing experimental literature in Sec. IV B, followed by a summary of our findings in Sec. V.

II. URANIUM-CRYSTALLINE PHASES

Uranium has a rich phase diagram. Below 935 K it is stable in the α phase (orthorhombic *Cmcm*), transforms to the β phase (bct), and changes to the stable γ phase (bcc) above 1045 K [18]. Although hcp-U does not occur among the bulk stable phases, it has been observed in thin films up to 100 Å (∼30 monolayers) [17], making it relevant to analyze the bulk hcp phase as well. We will focus on three types, α-, hcp-, and γ-U. Their lattice parameters and crystal structure are summarized in Table I and the x-y plane is defined according to Fig. 1. All parameters are experimental values [19,30,31], which we subsequently use for all electronic structure calculations.

*mh.wu@bristol.ac.uk

 ©2020 American Physical Society

TABLE I. Experimental lattice parameters of γ-, hcp-, and α-U used for the calculations.

Phase	a (Å)	b/a	c/a	y
γ (bcc)	3.467			
hcp	2.983		1.836	
α (orthorhombic)	2.836	2.075	1.741	0.1017

III. METHODS

For all electronic structure calculations we use the relativistic Korringa-Kohn-Rostoker Green's function method based on density functional theory [32–34]. The angular momentum cutoff is $l = 3$ and we used the local density approximation in the Vosko-Wilk-Nusair parametrization [35]. The impurity cluster contained 65 atoms for γ-U, 69 atoms for hcp-U, and 65 atoms for α-U. The spin-dependent transport is described by the intrinsic spin Hall effect, arising from the clean crystal, and the extrinsic spin Hall effect driven by impurity scattering. Here, we restrict the consideration to the extrinsic skew scattering ignoring the side-jump mechanism. This is a reasonable approximation in the dilute limit of impurity concentrations as has been shown previously [36]. The intrinsic SHE only depends on the electronic structure of the perfect crystal and arises from spin-orbit-induced near degeneracies and avoided crossings in the band structure. The equations are expressed within the semiclassical transport theory where the spin Hall conductivity (SHC) is described in terms of the Berry curvature [37,38], where we use its implementation in the relativistic KKR formalism [29,39]. The extrinsic SHE is driven by the scattering from weak structural disorder or dynamic perturbations coupled with a spin-orbit interaction of the electronic states. Here, we only consider the spin-dependent skew scattering of electrons at substitutional impurities captured in the semiclassical Boltzmann equation [27,40]. The detailed formalism for both approaches was described previously and here only the most relevant expressions are highlighted for convenience.

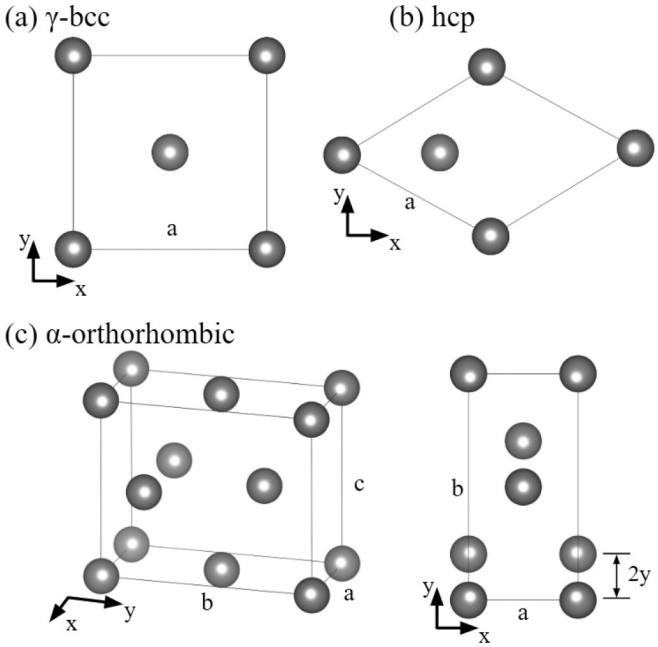

FIG. 1. Crystal structure of (a) γ-, (b) hcp-, and (c) α-U.

The intrinsic SHC is expressed via a Brillouin zone integral over the Berry curvature of all occupied states,

$$\sigma_{xy} = -\frac{e^2}{\hbar}\sum_n \int_{\mathrm{BZ}} \frac{d\mathbf{k}}{(2\pi)^3} f_n(E_F, \mathbf{k})\Omega_n^z(\mathbf{k}), \tag{1}$$

where the z component of the non-Abelian Berry curvature is given by

$$\begin{aligned}\boldsymbol{\Omega}_{ij}(\mathbf{k}) = i\langle\nabla_{\mathbf{k}} u_{i\mathbf{k}}| \times |\nabla_{\mathbf{k}} u_{j\mathbf{k}}\rangle \\ - i\sum_{l\in\Sigma}\langle\nabla_{\mathbf{k}} u_{i\mathbf{k}}|u_{l\mathbf{k}}\rangle \times \langle u_{l\mathbf{k}}|\nabla_{\mathbf{k}} u_{j\mathbf{k}}\rangle.\end{aligned} \tag{2}$$

The states i and j are from the set of degenerate states due to Kramers degeneracy induced by time and space inversion symmetry of the system. A detailed discussion of the method can be found in Ref. [29] (see also Ref. [41]).

For the extrinsic spin Hall effect (skew scattering) the semiclassical linearized Boltzmann equation is solved [27],

$$\boldsymbol{\Lambda}^n(\mathbf{k}) = \tau_{\mathbf{k}}^n\left[\mathbf{v}_{\mathbf{k}}^n + \sum_{\mathbf{k}'n'} P_{\mathbf{k}'n}^{n'n}\boldsymbol{\Lambda}^{n'}(\mathbf{k}')\right], \tag{3}$$

where $\boldsymbol{\Lambda}^n(\mathbf{k})$, $\tau_{\mathbf{k}}^n$, $\mathbf{v}_{\mathbf{k}}^n$, and $P_{\mathbf{k}'\mathbf{k}}^{n'n}$ are the mean free path, relaxation time, Fermi velocity, and scattering rate, respectively. All those quantities are directly calculated from the relativistic electronic structure code. After solving the linearized Boltzmann equation, the mean free path $\boldsymbol{\Lambda}^n(\mathbf{k})$ is used to calculate the spin conductivity in the zero-temperature limit,

$$\underline{\sigma}^s = \frac{e^2}{\hbar}\sum_n \frac{1}{(2\pi)^3}\iint_{E_{\mathbf{k}}=E_F} \frac{dS_n}{|\mathbf{v}_{\mathbf{k}}^n|} s_z^n(\mathbf{k})\mathbf{v}_{\mathbf{k}}^n \circ \boldsymbol{\Lambda}^n(\mathbf{k}). \tag{4}$$

The charge conductivity is expressed in the same way dropping $s_z^n(\mathbf{k})$. The spin expectation value s_z^n in the z direction implies we are considering the charge and spin transport in the x-y plane. Generally, other elements of the conductivity tensors might be nonzero and relevant. For cubic systems all other elements either vanish or are symmetry related [42]. We will come back to this point in the Sec. IV discussing α-U. The ratio of spin conductivity and charge conductivity is called the spin Hall angle (SHA),

$$\theta = \frac{\sigma_{yx}^S}{\sigma_{xx}}, \tag{5}$$

and is often used as a figure of merit quantifying the efficiency of charge-to-spin current conversion.

IV. RESULTS

A. Intrinsic and extrinsic spin Hall effect

In uranium the narrow $5f$ bands combined with the strong spin-orbit coupling significantly increases the number of near degeneracies enhancing the Berry curvature, the source of the intrinsic spin Hall conductivity. Figure 2 shows the intrinsic SHC σ_{yx}^s of the three phases as a function of energy. Surprisingly, all three show a rather similar functional dependence

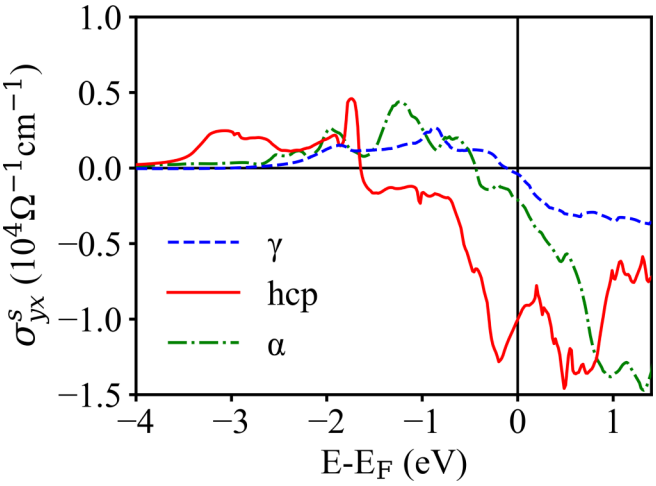

FIG. 2. The calculated intrinsic spin Hall conductivity σ^s_{yx} of γ-, hcp-, and α-U.

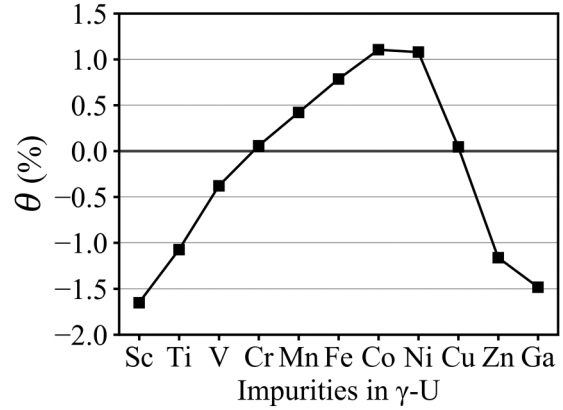

FIG. 3. The spin Hall angle of the γ-U doped with 3d transition metals. All conventionally magnetic atoms become nonmagnetic as impurity in γ-U.

with a roughly similar magnitude until ~ -0.8 eV below the Fermi energy. All of them start with positive conductivities at low energies, have a transition to negative values, and show some negative peaks at high energies. The key difference between the three distinct phases is the energy at which the SHC becomes significant, subsequently at which point the transition from positive to negative values happens, and resulting from that what the actual values at the Fermi energy are. Those values are summarized in Table II and highlight the dramatic change over two orders of magnitude going from the γ phase over the α to the hcp phase.

Experimental studies for the spin-dependent transport in U are sparse. At room temperature a value for the spin Hall angle of $\theta = 0.4\%$ was reported with a SHC of $\sigma^s_{yx} = 1.40 \times 10^2\ \Omega^{-1}\,\mathrm{cm}^{-1}$ [26]. This result is comparable to the value for γ-U instead of the experimentally expected phase of α-U. In addition, we found a negative sign of the SHC in all three phases relative to the sign in Pt (see Table II). However, from the experimental work it is not clear whether the sign was considered in detail. In order to derive the experimental parameters, the spin diffusion length of U was assumed to be 3 nm, the same as Pt, since no data for U were available [26]. This could potentially explain the gap between the theoretical and the experimental finding. In addition, structural inhomogeneities as well as the experiments performed at room temperatures will make any comparison to the theoretical results difficult. For reference we highlight the situation for Pt in Table II. While the reported theoretical values for σ^s_{yx} of Pt are of the order of $10^3\ \Omega^{-1}\,\mathrm{cm}^{-1}$, the experimentally observed values range from 0.5×10^3 to $3.5 \times 10^3\ \Omega^{-1}\,\mathrm{cm}^{-1}$. The importance of crystal quality in determining the transition between the intrinsic to the extrinsic regime in Pt has been highlighted in detail by Sagasta *et al.* [43]. Similarly, the effect of temperature has been studied for Pt in detail, showing a much smaller effect than in noble metals such as Au [44]. For uranium no further experimental work on the SHE exists, implying the transition between the superclean metal (dominance of extrinsic effects) and the moderately dirty regime (dominance of the intrinsic mechanism) is not clear from the experimental data. In the following we will consider the extrinsic mechanism to make predictions at which point such a transition should occur for the various phases of U. Nevertheless, it should be highlighted that σ^s_{yx} for hcp-U is two orders of magnitude larger than the experimental result. This suggests that metastable hcp-U is a viable choice in order to maximize the charge-to-spin current conversion in actual microscopic devices.

TABLE II. The comparison between our calculation of the intrinsic SHC and the experimental results for the longitudinal conductivity σ_{xx} and the spin Hall conductivity σ^s_{yx}. The experimental and theoretical results of Pt are given for reference. The measurement of all experimental references is the spin pumping method.

Material	σ_{xx} ($\Omega^{-1}\,\mathrm{cm}^{-1}$)	σ^s_{yx} ($\Omega^{-1}\,\mathrm{cm}^{-1}$)
γ		-4.02×10^2
hcp		-1.00×10^4
α		-2.12×10^3
Expt. U [26]	3.50×10^4	1.40×10^2
Theor. Pt [29,45–47]		1.3–3.2×10^3
Expt. Pt [48–53]	2.0–5.3×10^4	0.5–3.6×10^3

To understand the full picture of the SHE in U, we proceed to calculate the extrinsic SHC for the three U structures doped with a series of 3d transition metals as well as with Ga for its similar electronic configuration. For γ-U, interestingly, we find all doped impurities remain nonmagnetic, including conventionally magnetic elements, such as Fe, Co, and Ni. Figure 3 shows the SHA θ for the γ-U with the various substitutional impurities. Working in the dilute limit implies that all conductivities arising from impurity scattering will be inversely proportional to the impurity concentration leaving the SHA [Eq. (5)] to be concentration independent. The magnitude of SHA is the largest for the Sc impurity and decreases as the number of 3d electron increases for the impurity atom. The transition from negative to positive values occurs between V and Cr, at almost half filling of $Z_d = 4$ at the impurity site resulting from the self-consistent impurity solver. The SHA shows the largest positive value for the Co impurity ($Z_d = 8$)

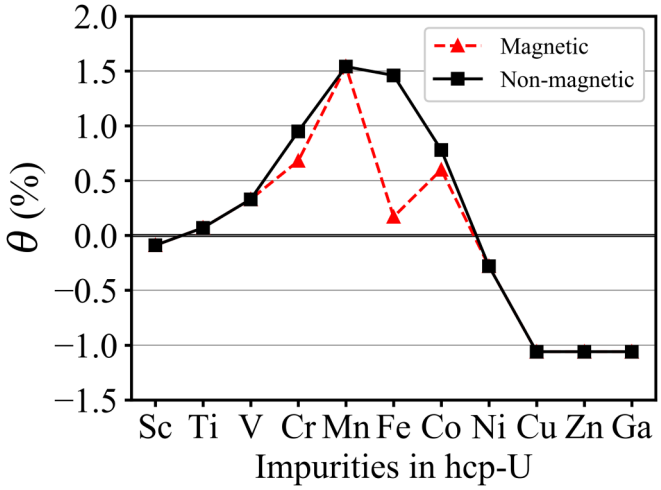

FIG. 4. The spin Hall angle for various substitutional 3*d* impurities in the hcp-U. Dashed line: Cr, Fe, and Co are magnetic impurities. Solid line: All impurities are forcedly nonmagnetic.

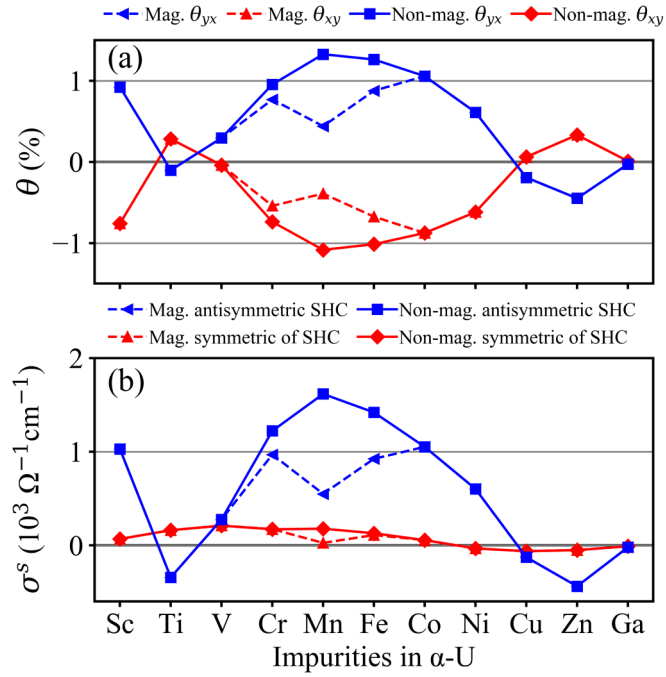

FIG. 5. (a) The spin Hall angle for various substitutional 3*d* impurities in the α-U. (b) The difference and average of the spin Hall conductivity in the x and y directions in α-U. Dashed lines show Cr, Mn, and Fe as magnetic impurities and for the solid lines all impurities are forcedly nonmagnetic.

and reverses to negative SHA beyond Cu, reaching -1.5% for the Ga impurity ($Z_d = 10.5$).

Surprisingly, the SHA trend is consistent with the prediction for Cu doped with 5*d* impurities reported by Fert *et al.* [54]. This concurrence demonstrates that the resonant scattering between $j = 5/2$ and $j = 3/2$ in d orbitals predominates in the transport properties of γ-U, despite the considerable f-orbital character of electrons in the valence bands as well as in the conduction bands. The contribution from d electrons can be attributed to the strong f-d hybridization in the uranium, allowing a certain charge transfer between f and d bands and consequently enhancing the coupling between the host atoms and impurities.

For hcp-U, the Cr, Fe, and Co impurities become magnetic, showing antiferromagnetic (AFM) coupling with the induced moments in the surrounding U. All other impurities remain nonmagnetic. In Fig. 4 we summarize the results for the SHA comparing the magnetic impurities to the same systems constrained to the nonmagnetic solution. For the constrained nonmagnetic systems, the trend is roughly similar to that of the γ-U, with the first sign change occurring between the Sc and Ti impurities already. The absolute values are very similar to the γ-U systems. When Cr, Fe, and Co are considered as magnetic impurities with corresponding moments of $1.99\mu_B$, $2.38\mu_B$, and $0.86\mu_B$, respectively, all SHA values decrease and for Fe, showing the largest moment, we find a dramatic decline from 1.5% to 0.2%. In Fig. 5(a) we show the corresponding results for the SHA in α-U with various 3*d* impurities. Given the reduced symmetries, the different elements, indicated as θ_{yx} and θ_{xy}, are no longer equivalent [42,55,56]. Nevertheless, their trends are almost identical. For α-U we find Cr, Mn, and Fe to exhibit magnetic moments of $1.09\mu_B$, $2.37\mu_B$, and $1.93\mu_B$, respectively, again ordering antiferromagnetically relative to the induced moments in the surrounding U. As before we show the nonmagnetically constrained systems for comparison. The principle structure is similar to the previous two phases with the maximum, in the nonmagnetic case, at the Mn impurity.

In order to highlight the reduced symmetry in α-U we summarize the symmetric and antisymmetric SHC, $\frac{1}{2}(\sigma^s_{yx} - \sigma^s_{xy})$ and $\frac{1}{2}(\sigma^s_{yx} + \sigma^s_{xy})$, respectively, in Fig. 5(b). In contrast to cubic systems, α-U shows a small but nonvanishing symmetric part for the SHC, but most of the structure visible in Fig. 5(a) is induced by the conventional antisymmetric contribution. Nevertheless, the symmetric contribution should be sizable enough to be picked up in a detailed experimental analysis.

For the 3*d* impurities we demonstrated that the d-orbital resonant scattering is predominant, giving the characteristic dependencies as introduced in Ref. [54]. While the predicted skew-scattering-induced SHAs are sizable, they do not exceed more than 1.5%. Previously, it has been shown that in simple heavy metallic hosts light impurities can induce large SHAs [27]. In Fig. 6 we present our results for a number of light elements in comparison to the 3*d* series as well as Mo. All impurities in the γ-U remain nonmagnetic while for hcp-U Fe and Ni and for α-U Fe become magnetic. Given that the symmetric contributions are small in α-U we present σ^s_{yx} only. The results for B, C, and N are similar to the first few elements of the 3*d* series and no drastic enhancement can be identified. Not surprisingly, the SHA for Mo, a 4*d* impurity with roughly the same charge as Cr ($Z_d = 5$), shows roughly the same SHA to Cr.

While B and C impurities can induce a large SHA comparable to Fe, Co, and Ni in γ- and hcp-U, the corresponding SHA is suppressed in α-U. Evidently, the simple relation of the large relative change of the SOC of the host versus the impurity as identified of simple metals [27] does not hold for the far more complex electronic structure of the various U

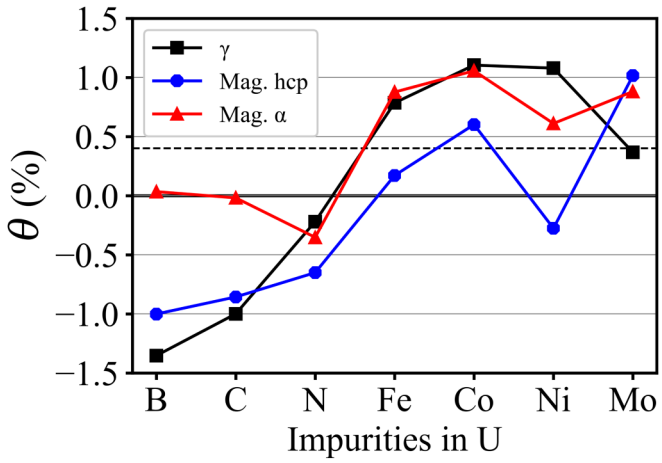

FIG. 6. The comparison of the spin Hall angle of the γ-, hcp-, and α-U doped from light to moderately heavy impurities. The Fe and Co in the hcp-U and Fe in the α-U are magnetic. The dashed line is indicating the experimentally found SHA [26].

crystalline phases where predictions from simple qualitative models fail. The experimental SHA [26], θ, is indicated as a dashed line in Fig. 6, showing reasonable agreement with our quantitative predictions.

B. Spin diffusion length and dilute concentration

In our calculations, the extrinsic SHA for α-U is consistent with the experimental observation while our calculated intrinsic SHC of α-U is one order of magnitude too large. For further insight into the spin-dependent transport in realistic U systems, we analyze the spin diffusion length and the total spin Hall angle in the dilute limit combining extrinsic and intrinsic contributions. In a free-electron model, the spin diffusion can be expressed as [28,57,58]

$$l_{\mathrm{sf}} = \sqrt{\frac{3}{2}}\frac{\pi}{k_F^2 G_0}\sqrt{\frac{\tau_{\mathrm{sf}}}{\tau}}\sigma_{xx}^{\mathrm{expt}}, \tag{6}$$

where k_F, G_o, τ_{sf}, τ, and $\sigma_{xx}^{\mathrm{expt}}$ are the Fermi wave vector, the conductance quantum of $\frac{2e^2}{h}$, the spin-flip scattering time, the momentum relaxation time, and the longitudinal charge conductivity, respectively.

Measuring the impurity concentration in experiments is challenging. However, in the dilute limit the concentration is inversely proportional to the longitudinal charge conductivity [28,59,60], suggesting that we can estimate an experimental impurity concentration as

$$c_{\mathrm{expt}} = \frac{\sigma_{xx}^{\mathrm{calc}}}{\sigma_{xx}^{\mathrm{expt}}} c_0, \tag{7}$$

where c_0 is the nominal impurity concentration of 1 at. % in our calculations for each structure. To estimate l_{sf} and c_{expt}, we assume $\sigma_{xx}^{\mathrm{expt}} = 3.5 \times 10^{-2}$ $(\mu\Omega\,\mathrm{cm})^{-1}$ of α-U [26] for all structures since no experimental data are available for $\sigma_{xx}^{\mathrm{expt}}$ in hcp-U and γ-U.

In principle, each impurity will induce a different spin diffusion length l_{sf} and σ_{xx}, but given the strong SOC of U, the results are dominated by the electronic structure of the host. All values are summarized in Table III, showing a clear distinction between the crystalline phases. While for the γ phase we find the 3 nm assumed for the experimental analysis [26], we predict the spin diffusion lengths l_{sf} for hcp-U and α-U to be 5 and 6.5 nm, respectively, almost two times larger. Reevaluating the experiment considering the larger spin diffusion length of $l_{\mathrm{sf}} = 6.5$ nm we obtain a SHA of $\theta = 0.38\%$ within the range of the originally presented value of 0.4%. This very weak change could not explain the discrepancy between theory and experiment.

TABLE III. The range of the spin diffusion length l_{sf} and the experimental concentration for different impurities in the γ-, hcp-, and α-U. These two quantities are estimated using the calculated results of the relaxation time with the experimental conductivity of 3.5×10^{-2} $(\mu\,\Omega\,\mathrm{cm})^{-1}$ [26].

Phase	l_{sf} (nm)	c_{expt} (%)	k_F (nm^{-1})	τ (fs)	τ_{sf} (10^{-3} fs)
γ	∼3	5–8	11.06	21.6–42.1	4.87–9.24
hcp	∼5	1.8–3.5	8.03	22.7–49.2	5.74–13.9
α	∼6.5	2.5–5.0	7.79	20.6–42.0	4.41–9.09

Estimating the necessary impurity concentration to reach the experimental longitudinal conductivities, assuming just one class of impurities present, we find, for γ-U, $c_{\mathrm{expt}} =$ 5%–8%, about 1.5 times larger than that of hcp-U and α-U. The concentrations of hcp-U vary between 1.8% and 3.5%, comparable to that of $c_{\mathrm{expt}} = 2.5\%$–$5.0\%$ of α-U, even though these two structures have significantly different trends and magnitudes for the SHA. The high concentration for γ-U indicates that it is unlikely that the experimental system is based on ideal γ-U since a rather unrealistically large impurity concentration or other large disorder potential would be needed. However, in the films the predominantly polycrystalline structures are difficult to describe from a theoretical perspective. For α- and hcp-U the impurity concentrations are in a reasonable range easily present in bilayered structures used in spin-pumping experiments.

In order to understand whether extrinsic or intrinsic effects dominate the different crystalline phases we summarize the calculated extrinsic longitudinal conductivities $\sigma_{xx}^{\mathrm{ext}}$ and the absolute values of the SHC $|\sigma_{yx}^{s(\mathrm{ext})}|$ both at an impurity concentration of $c_0 = 1$ at. % in Table IV. For the γ-U we find $\sigma_{xx}^{\mathrm{ext}}$ to be up to two times larger than that of hcp-U and α-U, which is directly linked to the nominal impurity concentration needed to reach the experimentally found longitudinal conductivity as highlighted in Table III. Given those conductivities and concentrations one would assume that we

TABLE IV. The range of calculated electrical conductivities σ_{xx}, spin Hall conductivities σ_{yx}^{s}, and the total spin Hall angle θ^{tot} combining the intrinsic σ_{yx}^{s} from Table II with the extrinsic results to estimate the total spin Hall angle θ^{tot}.

Phase	σ_{xx} $(\mu\Omega\,\mathrm{cm})^{-1}$	$\lvert\sigma_{yx}^{s(\mathrm{ext})}\rvert$ $(\mu\Omega\,\mathrm{cm})^{-1}$	θ^{tot} (%)
γ	17.3–30.0 × 10^{-2}	0.8–48.1 × 10^{-4}	0.01–2.3
hcp	6.2–12.4 × 10^{-2}	1.1–10.6 × 10^{-4}	27.5–30.1
α	8.8–17.7 × 10^{-2}	0.2–17.9 × 10^{-4}	5.6–7.1

are in the moderately dirty regime where in most cases the intrinsic mechanism will dominate [43,61,62]. To validate this point we calculate the absolute values of the total SHA, $\theta^{\text{tot}} = |(c_{\text{expt}} \times \sigma_{yx}^{s(\text{int})} + \sigma_{yx}^{s(\text{ext})})/\sigma_{xx}^{\text{ext}}|$ in Table IV for all three phases. Here, we assume, as discussed above, impurity concentrations such that the resulting theoretical conductivities match the experimentally found conductivity of 3.5×10^{-2} $(\mu\Omega\,\text{cm})^{-1}$ [26]. The expression indicates clearly how in the moderately dirty regime the intrinsic mechanism becomes more and more dominant as the impurity concentration increases. Nevertheless, depending on the size of the individual contributions they might be comparable.

This is precisely what happens for γ-U, where the extrinsic SHC ranges from 0.8×10^{-4} $(\mu\Omega\,\text{cm})^{-1}$ to 4.8×10^{-3} $(\mu\Omega\,\text{cm})^{-1}$ sometimes significantly larger than the intrinsic SHC of $|\sigma_{yx}^{s(\text{int})}| = 4.02 \times 10^{-4}$ $(\mu\Omega\,\text{cm})^{-1}$. Therefore its total SHA, $\theta^{\text{tot}} = 0.01\%$–$2.25\%$, is in many situations dominated by the extrinsic mechanism. In contrast, for the hcp-U, the extrinsic SHCs are two orders of magnitude smaller than $|\sigma_{yx}^{s(\text{int})}|$ and the total SHA, $\theta^{\text{tot}} = 27.5\%$–$30.1\%$, is induced by the intrinsic mechanism creating a giant SHE.

For the α-U, we find $|\sigma_{yx}^{s(\text{ext})}|$ to vary in a broad range over three orders of magnitude from 2.0×10^{-5} $(\mu\Omega\,\text{cm})^{-1}$ to 1.8×10^{-3} $(\mu\Omega\,\text{cm})^{-1}$. However, the highest value is still smaller than the intrinsic SHC and the total $\theta^{\text{tot}} = 5.6\%$–$7.1\%$ is considerably larger than the extrinsic SHA of around 1%. Combining all our quantitative results, our prediction is that in the experimental thin films γ-U is the predominant phase. On the other hand, a giant SHA can be induced exploiting hcp-U.

V. SUMMARY

In summary, we have applied a DFT-based first-principles Green's function method to analyze the charge-to-spin current conversion efficiency of various U phases. Predicting the relevant parameters, intrinsic SHC, extrinsic SHC, longitudinal conductivity, and spin diffusion length, we found dramatic differences between the distinct crystalline phases despite all effects being derived from nominally the same large atomic spin-orbit coupling. With these results we were able to give a possible explanation for the surprisingly low spin Hall effect found experimentally. Our calculations suggest the experimental system is based on γ-U rather than the experimentally expected α-U. Furthermore, we have demonstrated that hcp-U shows the largest SHA of up to 30% driven by the gigantic intrinsic contribution.

On the other hand, the results of the extrinsic SHC indicate that the resonant scattering from d-orbital electrons is predominant for the $3d$ transition element impurities. Magnetism, induced by the impurities, led in all cases to a reduction of the SHA correlated with the magnitude of the induced magnetic moment.

In addition, the predicted spin diffusion lengths and longitudinal conductivities compare quantitatively well to the experimental assumptions. We estimate the spin diffusion length to range from 3 nm for γ-U to 6.5 nm for α-U. Combining the intrinsic as well as the extrinsic results we were able to predict the dominance of the extrinsic mechanism for the γ phase, whereas for the α and hcp phase the intrinsic mechanism is dominant.

Combining all our results we encourage experimentalists to focus on the growth of hcp-U in thin-film geometry to harness the high efficiency of the charge-to-spin current conversion of up to 30% with a spin diffusion length of 5 nm, which is a typical value for charge-to-spin conversion materials.

ACKNOWLEDGMENTS

This work was sponsored by EPSRC Grant No. EP/N509619/1. The authors are grateful to Tom G. Saunderson for fruitful discussions.

[1] D. Apalkov, B. Dieny, and J. M. Slaughter, Proc. IEEE **104**, 1796 (2016).
[2] Y. Ando, Jpn. J. Appl. Phys. **54**, 070101 (2015).
[3] G. Zhao and W. Prenat, *Spintronics-Based Computing* (Springer, Berlin, 2015).
[4] A. Fert and H. Jaffrès, Phys. Rev. B **64**, 184420 (2001).
[5] G. Schmidt, D. Ferrand, L. W. Molenkamp, A. T. Filip, and B. J. van Wees, Phys. Rev. B **62**, R4790 (2000).
[6] I. M. Miron, K. Garello, G. Gaudin, P.-J. Zermatten, M. V. Costache, S. Auffret, S. Bandiera, B. Rodmacq, A. Schuhl, and P. Gambardella, Nature (London) **476**, 189 (2011).
[7] J. Sinova, D. Culcer, Q. Niu, N. A. Sinitsyn, T. Jungwirth, and A. H. MacDonald, Phys. Rev. Lett. **92**, 126603 (2004).
[8] N. Nagaosa, J. Sinova, S. Onoda, A. H. MacDonald, and N. P. Ong, Rev. Mod. Phys. **82**, 1539 (2010).
[9] H. L. Wang, C. H. Du, Y. Pu, R. Adur, P. C. Hammel, and F. Y. Yang, Phys. Rev. Lett. **112**, 197201 (2014).
[10] C. Du, H. Wang, F. Yang, and P. C. Hammel, Phys. Rev. B **90**, 140407(R) (2014).
[11] J. Sinova, S. O. Valenzuela, J. Wunderlich, C. H. Back, and T. Jungwirth, Rev. Mod. Phys. **87**, 1213 (2015).
[12] K. T. Moore and G. van der Laan, Rev. Mod. Phys. **81**, 235 (2009).
[13] J. Smith and E. Kmetko, J. Less-Common Met. **90**, 83 (1983).
[14] P. Söderlind, O. Eriksson, B. Johansson, J. M. Wills, and A. M. Boring, Nature (London) **374**, 524 (1995).
[15] L. Berbil-Bautista, T. Hänke, M. Getzlaff, R. Wiesendanger, I. Opahle, K. Koepernik, and M. Richter, Phys. Rev. B **70**, 113401 (2004).
[16] Y. G. Hao, O. Eriksson, G. W. Fernando, and B. R. Cooper, Phys. Rev. B **47**, 6680 (1993).
[17] S. L. Molodtsov, J. Boysen, M. Richter, P. Segovia, C. Laubschat, S. A. Gorovikov, A. M. Ionov, G. V. Prudnikova, and V. K. Adamchuk, Phys. Rev. B **57**, 13241 (1998).
[18] C.-S. Yoo, H. Cynn, and P. Söderlind, Phys. Rev. B **57**, 10359 (1998).
[19] R. Springell, B. Detlefs, G. H. Lander, R. C. C. Ward, R. A. Cowley, N. Ling, W. Goetze, R. Ahuja, W. Luo, and B. Johansson, Phys. Rev. B **78**, 193403 (2008).

[20] L. Fast, O. Eriksson, B. Johansson, J. M. Wills, G. Straub, H. Roeder, and L. Nordström, Phys. Rev. Lett. **81**, 2978 (1998).
[21] N. Stojić, J. W. Davenport, M. Komelj, and J. Glimm, Phys. Rev. B **68**, 094407 (2003).
[22] A. Laref, E. Şaşioglu, and L. M. Sandratskii, J. Phys.: Condens. Matter **18**, 4177 (2006).
[23] S. D. Brown, L. Bouchenoire, P. Thompson, R. Springell, A. Mirone, W. G. Stirling, A. Beesley, M. F. Thomas, R. C. C. Ward, M. R. Wells, S. Langridge, S. W. Zochowski, and G. H. Lander, Phys. Rev. B **77**, 014427 (2008).
[24] R. Springell, S. W. Zochowski, R. C. C. Ward, M. R. Wells, S. D. Brown, L. Bouchenoire, F. Wilhelm, S. Langridge, W. G. Stirling, and G. H. Lander, J. Phys.: Condens. Matter **20**, 215230 (2008).
[25] R. Springell, S. W. Zochowski, R. C. C. Ward, M. R. Wells, S. D. Brown, L. Bouchenoire, F. Wilhelm, S. Langridge, W. G. Stirling, and G. H. Lander, J. Phys.: Condens. Matter **20**, 215229 (2008).
[26] S. Singh, M. Anguera, E. del Barco, R. Springell, and C. W. Miller, Appl. Phys. Lett. **107**, 232403 (2015).
[27] M. Gradhand, D. V. Fedorov, P. Zahn, and I. Mertig, Phys. Rev. Lett. **104**, 186403 (2010).
[28] M. Gradhand, D. V. Fedorov, P. Zahn, and I. Mertig, Phys. Rev. B **81**, 245109 (2010).
[29] M. Gradhand, D. V. Fedorov, F. Pientka, P. Zahn, I. Mertig, and B. L. Györffy, Phys. Rev. B **84**, 075113 (2011).
[30] A. S. Wilson and R. E. Rundle, Acta Crystallogr. **2**, 126 (1949).
[31] C. S. Barrett, M. H. Mueller, and R. L. Hitterman, Phys. Rev. **129**, 625 (1963).
[32] J. Korringa, Physica **13**, 392 (1947).
[33] W. Kohn and N. Rostoker, Phys. Rev. **94**, 1111 (1954).
[34] M. Gradhand, M. Czerner, D. V. Fedorov, P. Zahn, B. Y. Yavorsky, L. Szunyogh, and I. Mertig, Phys. Rev. B **80**, 224413 (2009).
[35] S. H. Vosko, L. Wilk, and M. Nusair, Can. J. Phys. **58**, 1200 (1980).
[36] S. Lowitzer, M. Gradhand, D. Ködderitzsch, D. V. Fedorov, I. Mertig, and H. Ebert, Phys. Rev. Lett. **106**, 056601 (2011).
[37] D. Xiao, M.-C. Chang, and Q. Niu, Rev. Mod. Phys. **82**, 1959 (2010).
[38] M. V. Berry, Proc. R. Soc. London, Ser. A **392**, 45 (1984).
[39] M. Gradhand, D. V. Fedorov, F. Pientka, P. Zahn, I. Mertig, and B. L. Györffy, J. Phys.: Condens. Matter **24**, 213202 (2012).
[40] M. Gradhand, D. V. Fedorov, P. Zahn, and I. Mertig, Phys. Rev. B **81**, 020403(R) (2010).
[41] Please note that we are using the opposite sign conventions to Ref. [29] consistent with the sign convention of Ref. [27]. Within this convention the intrinsic spin Hall conductivity σ_{yx}^{S} for Pt is positive.
[42] M. Seemann, D. Ködderitzsch, S. Wimmer, and H. Ebert, Phys. Rev. B **92**, 155138 (2015).
[43] E. Sagasta, Y. Omori, M. Isasa, M. Gradhand, L. E. Hueso, Y. Niimi, Y. C. Otani, and F. Casanova, Phys. Rev. B **94**, 060412(R) (2016).
[44] M. Isasa, E. Villamor, L. E. Hueso, M. Gradhand, and F. Casanova, Phys. Rev. B **91**, 024402 (2015).
[45] G. Y. Guo, S. Murakami, T.-W. Chen, and N. Nagaosa, Phys. Rev. Lett. **100**, 096401 (2008).
[46] T. Tanaka, H. Kontani, M. Naito, T. Naito, D. S. Hirashima, K. Yamada, and J. Inoue, Phys. Rev. B **77**, 165117 (2008).
[47] L. Wang, R. J. H. Wesselink, Y. Liu, Z. Yuan, K. Xia, and P. J. Kelly, Phys. Rev. Lett. **116**, 196602 (2016).
[48] K. Ando, S. Takahashi, J. Ieda, Y. Kajiwara, H. Nakayama, T. Yoshino, K. Harii, Y. Fujikawa, M. Matsuo, S. Maekawa, and E. Saitoh, J. Appl. Phys. **109**, 103913 (2011).
[49] W. Zhang, V. Vlaminck, J. E. Pearson, R. Divan, S. D. Bader, and A. Hoffmann, Appl. Phys. Lett. **103**, 242414 (2013).
[50] A. Azevedo, L. H. Vilela-Leão, R. L. Rodríguez-Suárez, A. F. Lacerda Santos, and S. M. Rezende, Phys. Rev. B **83**, 144402 (2011).
[51] V. Vlaminck, J. E. Pearson, S. D. Bader, and A. Hoffmann, Phys. Rev. B **88**, 064414 (2013).
[52] Z. Feng, J. Hu, L. Sun, B. You, D. Wu, J. Du, W. Zhang, A. Hu, Y. Yang, D. M. Tang, B. S. Zhang, and H. F. Ding, Phys. Rev. B **85**, 214423 (2012).
[53] X. Tao, Q. Liu, B. Miao, R. Yu, Z. Feng, L. Sun, B. You, J. Du, K. Chen, S. Zhang, L. Zhang, Z. Yuan, D. Wu, and H. Ding, Sci. Adv. **4**, eaat1670 (2018).
[54] A. Fert and P. M. Levy, Phys. Rev. Lett. **106**, 157208 (2011).
[55] F. Freimuth, S. Blügel, and Y. Mokrousov, Phys. Rev. Lett. **105**, 246602 (2010).
[56] Y. Mokrousov, H. Zhang, F. Freimuth, B. Zimmermann, N. H. Long, J. Weischenberg, I. Souza, P. Mavropoulos, and S. Blügel, J. Phys.: Condens. Matter **25**, 163201 (2013).
[57] T. Valet and A. Fert, Phys. Rev. B **48**, 7099 (1993).
[58] S. Takahashi and S. Maekawa, Physica C **437-438**, 309 (2006).
[59] I. Mertig, Rep. Prog. Phys. **62**, 237 (1999).
[60] N. A. Sinitsyn, A. H. MacDonald, T. Jungwirth, V. K. Dugaev, and J. Sinova, Phys. Rev. B **75**, 045315 (2007).
[61] S. Onoda, N. Sugimoto, and N. Nagaosa, Phys. Rev. Lett. **97**, 126602 (2006).
[62] X.-J. Liu, X. Liu, and J. Sinova, Phys. Rev. B **84**, 165304 (2011).